Exploiting Distributed IRSs for Enabling SWIPT

Diluka Loku Galappaththige, *Student Member, IEEE* and Gayan Aruma Baduge, *Senior Member, IEEE*

***Abstract*—In this paper, the feasibility of boosting the performance of simultaneous wireless information and power transfer (SWIPT) via distributed intelligent reflecting surfaces (IRSs) is investigated. The performance bounds of a distributed IRSs-assisted SWIPT set-up are derived by adopting practically viable discrete phase-shifts for time-switching and power-splitting protocols with non-linear energy harvesting circuitry. The optimal received signal power and optimal signal-to-noise ratio (SNR) are derived by controlling the phase-shifts of passive reflectors at each IRS. Thereby, closed-form approximations/bounds for the achievable rate, harvested energy, and rate-energy trade-off are derived for Nakagami-m fading. The accuracy of our analysis is validated by presenting a rigorous set of Monte-Carlo simulations. Our numerical results reveal that the distributed IRSs-assisted communication set-ups can boost the performance of SWIPT in the next-generation wireless systems.**

***Index Terms*—Distributed IRSs, SWIPT, Performance analysis**

I. Introduction

Intelligent reflecting surfaces (IRSs) are made of artificially engineered electromagnetic (EM) meta-materials and which consist of a large number of tiny passive reflectors [1], [2]. These reflectors can introduce distinct yet controllable delays to their impinging EM waves, and this in turn results in smartly adjustable phase-shifts. With the aid of IRSs, the propagation properties of EM waves can be reconfigured to enable a smart propagation environment. Towards this end, IRSs can be used to boost the signal-to-noise ratio (SNR) of a communication channel by enabling constructive EM wave combining at a desired destination [3], [4]. When the physical objects surrounding a receiver are coated with IRSs, the received signal power can similarly be boosted, and this paves a way to effectively harness the benefits of simultaneous wireless information and power transfer (SWIPT) [5]–[7].

By exploiting the broadcast nature of EM wave propagation, the concept of SWIPT has recently emerged [5], [6]. In particular, SWIPT techniques can be leveraged to prolong the battery life of low-power wireless nodes such as Internet-of-things [5], [6]. Instead of having conventional separated information/energy receiver architectures [5], two low-complexity co-located receiver schemes, namely the power-splitting (PS) and the time-switching (TS) receivers have been proposed for enabling SWIPT in wireless systems [6].

In [1], [2], architectural and theoretical foundations of IRS-assisted communication are discussed. References [3], [4] study the feasibility of deploying distributed IRSs by deriving the fundamental performance metrics over Nakagami-m fading. In [7], a low-complexity iterative algorithm based on the classical block coordinate descent (BCD) technique is proposed for optimizing the transmit precoding at a base-station and the phase-shifts at the IRS to enhance the performance of energy and information receivers in an IRS-assisted SWIPT multiple-input multiple-output (MIMO) system. Reference [8] proposes solutions to critical design challenges associated with IRS, and future research directions are discussed. In [9], a survey on IRS-assisted SWIPT is presented for tackling the operational challenges, including passive beamforming, channel estimation, and deployment. In [10], the secrecy sum rate maximization of IRS-assisted SWIPT MIMO channel is investigated by jointly optimizing the precoder matrix, artificial noise covariance, and phase-shifts at IRSs. Thereby, the majorization-minimization and complex circle manifold methods are proposed based on an inexact-BCD algorithm to improve the system performance. Reference [11] investigates the weighted sum rate maximization of IRS-SWIPT communication by investigating the performance of a single IRS-assisted system. In [12], the energy efficiency for a secure IRS-assisted SWIPT system is investigated by exploiting an alternative optimization method. Reference [13] investigates the performance of a single IRS-assisted SWIPT system for both quantized and continuous phase-shifts at the IRS over Rayleigh fading.

The concept of IRS is originally envisioned for coating geographically distributed objects within a propagation environment, and this enables smart wireless communications through distributed IRSs. However, a common attribute of the aforementioned/related prior research on IRS-assisted SWIPT [7], [10]–[13] is that the corresponding system models consist of a single IRS set-up. Although the notion of distributed IRSs is explored in [3], [4] for the sole purpose of information transmission, to the best of our knowledge, the fundamental performance bounds of a distributed IRSs-assisted SWIPT set-up have not yet been investigated in the open literature. Towards this end, we fill this important gap in the literature by establishing the fundamental performance metrics pertaining to a SWIPT-enabled distributed IRSs set-up over Nakagami-m fading. Specifically, the harvested energy (HE) with a non-linear circuitry, achievable rate bounds, and energy-rate trade-off are derived for TS and PS protocols by adopting discrete phase-shift adjustments at the distributed IRSs. We validate the accuracy of our analysis by comparing the exact performance metrics through Monte-Carlo simulations and our analytical counterparts. We investigate the feasibility of deploying distributed IRSs for enhancing the performance of SWIPT for the next-generation wireless systems by presenting insightful numerical results.

Notation: For a random variable (RV) X, $\mathbb{E}[X]$ and $\mathbb{V}\mathrm{ar}[X]$ denote the expectation and variance. A complex-valued circularly symmetric Gaussian distributed RV X with μ_X mean and σ_X^2 variance is denoted by $X \sim \mathcal{CN}(\mu_X, \sigma_X^2)$. The notation $\mathbf{x}^T$ represents the transpose of $\mathbf{x}$ and $C^n = \{0, 1, \cdots, n\}$.

The authors are with the School of Electrical, Computer, and Biomedical Engineering, Southern Illinois University, Carbondale, IL, USA, Email: {diluka.lg,gayan.baduge}@siu.edu.

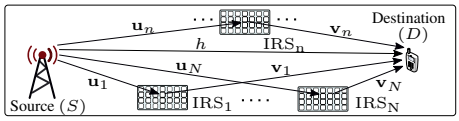

Fig. 1. System model - A distributed IRS-assisted SWIPT set-up.

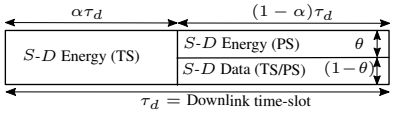

Fig. 2. A generalized transmission frame structure for TS and PS protocols.

II. System, channel and signal models

A. System and channel model

We consider a distributed IRSs-assisted SWIPT set-up. A single-antenna source (S) serves a single-antenna destination (D) with information and power through the direct channel and reflected channels of N distributed IRSs, each having L passive reflectors (see Fig. 1). We generalize the energy harvesting model at D by adopting both TS and PS protocols (see Fig. 2). It is assumed that the phase-shifts of incident EM waves at the reflectors of IRSs can be smartly adjusted to enable a constructive combining of the received signals at D. For the sake of notation brevity, we denote the set of IRSs as $\mathcal{N}=\{1,\cdots,N\}$, and the set of reflectors as $\mathcal{L}=\{1,\cdots,L\}$. The direct channel between S and D is represented by h. The channel between S and the lth reflector of the nth IRS is represented by u_{nl}. The channel between the lth reflector of the nth IRS and D is denoted by v_{nl}. The envelopes of these channels are modeled to be independent Nakagami-m distributed so that a myriad of fading conditions can be realized by varying the shape parameter (m). The polar form of complex channel coefficients is given by

$$g = \beta_g \mathrm{e}^{j\theta_g}, \tag{1}$$

where $g\in\{h,u_{nl},v_{nl}\}$ and $n\in\mathcal{N}$, $l\in\mathcal{L}$. Moreover, β_g denotes the envelope and θ_g is the phase of g. The probability distribution function (PDF) of β_g follows Nakagami-m distribution and is given as $f_{\beta_g}(x)=2m_g^{m_g}x^{2m_g-1}/(\Gamma(m_g)\xi_g^{m_g})\mathrm{e}^{-m_g x^2/\xi_g}$ [14], where m_g and $\xi_g=m_g\zeta_g$ denote the shape parameter and scaling parameter, respectively, while ζ_g accounts for the path-attenuation/large-scale fading of the channel (g) in (1). Moreover, for the reflective channels u_{nl} and v_{nl}, $m_{g'_{nl}}=m_{g'}$ and $\xi_{g'_{nl}}=m_{g'_{nl}}\zeta_{g'_{nl}}=\xi_{g'_n}$, where $g'\in\{u,v\}$. Since the reflectors are co-located, the large-scale fading parameters are assumed to be the same for a given IRS. However, different IRSs have distinct large-scale fading parameters.

SWIPT is performed by using TS and/or PS receiver structures. The coherence interval (τ_c) is allocated for S-to-D (downlink) transmission (τ_d). To harvest energy and receive payload data, τ_d is further divided into two orthogonal portions depending on the TS factors (α) (see Fig. 2). The first $\alpha\tau_d$ portion is allocated for S-to-D power transfer via the TS protocol. In the remaining $(1-\alpha)\tau_d$ portion, the PS protocol is adopted, and hence, the received signal power is split into two streams by using a power splitter having a PS ratio of $\theta:1-\theta$. Then, the received signal is passed through the energy harvester and the information decoder.

B. Non-linear energy harvesting model

It has been shown that the HE at a rectenna is a non-linear function of its received power [15]. To capture this non-linear operating characteristic, the HE is modeled as [15]

$$\Psi_{EH}\left(P_r\right)=\left[\lambda\left(1-\mathrm{e}^{-\mu P_r}\right)\Big/\left(1+\mathrm{e}^{-\mu(P_r-\omega)}\right)\right]^+, \tag{2}$$

where $\Psi_{EH}\left(P_r\right)$ is the HE, which is a non-linear function of P_r, and $[z]^+=\max(0,z)$. Moreover, λ, μ, and ω are used to model the corresponding non-linearities of the energy harvesting circuitry. Following [15], these parameters are set as $\lambda=20\,\mathrm{mW}$, $\mu=6400\,/\mu\mathrm{W}$, and $\omega=2.9\,\mu\mathrm{W}$.

C. Signal model

The received signal at D is a combination of the transmitted signal at S through the direct channel and reflected channels of N distributed IRSs. The signal received at D is written as

$$r=\sqrt{P}\left(h+\sum\nolimits_{n\in\mathcal{N}}\mathbf{v}_n^T\mathbf{\Theta}_n\mathbf{u}_n\right)x+w, \tag{3}$$

where the transmitted signal at S is denoted by x, which satisfies $\mathbb{E}\left[|x|^2\right]=1$, P represents the transmit power, and $w\sim\mathcal{CN}(0,\sigma_w^2)$ is an additive white Gaussian noise (AWGN) at D. Here, the channel vector between S and the nth IRS is denoted by $\mathbf{u}_n=[u_{n1},\cdots,u_{nl},\cdots,u_{nL}]^T\in\mathbb{C}^{L\times 1}$, while $\mathbf{v}_n^T=[v_{n1},\cdots,v_{nl},\cdots,v_{nL}]\in\mathbb{C}^{1\times L}$ represents the channel vector between the nth IRS and D. The reflective properties of the nth IRS is captured by a diagonal matrix, $\mathbf{\Theta}_n=\mathrm{diag}\left(\eta_{n1}\mathrm{e}^{j\theta_{n1}},\cdots,\eta_{nl}\mathrm{e}^{j\theta_{nl}},\cdots,\eta_{nL}\mathrm{e}^{j\theta_{nL}}\right)\in\mathbb{C}^{L\times L}$, where $\eta_{nl}\mathrm{e}^{j\theta_{nl}}$ denotes the complex-valued reflection coefficient at the lth reflector of the nth IRS. Moreover, η_{nl} and θ_{nl} are the magnitude of attenuation and phase-shift, respectively. Thus, by exploiting the properties of $\mathbf{\Theta}_n$, the signal received at D in (3) is rearranged as

$$r=\sqrt{P}\Big(\beta_h\mathrm{e}^{j\theta_h}+\sum\nolimits_{n\in\mathcal{N}}\sum\nolimits_{l\in\mathcal{L}}\eta_{nl}\beta_{v_{nl}}\beta_{u_{nl}}\mathrm{e}^{j\phi_{nl}}\Big)x+w, \tag{4}$$

where $\phi_{nl}=\theta_{nl}+\theta_{v_{nl}}+\theta_{u_{nl}}$.

D. The received signal power

The received signal power at D is computed by using the received signal (4) as

$$P_r=P\left|\beta_h\mathrm{e}^{j\theta_h}+\sum\nolimits_{n\in\mathcal{N}}\sum\nolimits_{l\in\mathcal{L}}\eta_{nl}\beta_{v_{nl}}\beta_{u_{nl}}\mathrm{e}^{j\phi_{nl}}\right|^2. \tag{5}$$

Thereby, the received signal power at D is maximized by allowing a constructive combining of NL signal terms inside the summation of (5) and the signal received through the direct channel [16]. Toward this end, the phases of the double summation in (5) can be smartly adjusted to have a constructive combining of the received signals through the direct and reflected channels. Thus, the optimal choice of θ_{nl} to enable a constructive addition at D is given by [16]

$$\theta_{nl}^*=\underset{-\pi\le\theta_{nl}\le\pi}{\mathrm{argmax}}\ P_r=\theta_h-(\theta_{v_{nl}}+\theta_{u_{nl}}),\ \text{for } n\in\mathcal{N}, l\in\mathcal{L}. \tag{6}$$

The optimal received signal power at D is derived as

$$P_{r,c}^*=P\left|\beta_h+\sum\nolimits_{n\in\mathcal{N}}\sum\nolimits_{l\in\mathcal{L}}\eta_{nl}\beta_{v_{nl}}\beta_{u_{nl}}\right|^2. \tag{7}$$

E. Effect of discrete phase-shits

In practice, adopting continuous phase-shifts at the IRSs can be infeasible due to hardware limitations. To circumvent this, we adopt discrete phase-shifts through phase-shift quantization. It is assumed that the IRS controller can select discrete phases from a limited number of quantized phases. Thus, the selected discrete phase for the lth reflector of the nth IRS is given as $\hat{\theta}^*_{nl} = \pi\kappa/2^{B-1}$, where B represents the number of quantization bits, $\kappa = \underset{q\in\{0,\pm1,\cdots,\pm2^{B-1}\}}{\operatorname{argmax}} |\theta^*_{nl} - \pi q/2^{B-1}|$, and θ^*_{nl} is the optimal phase-shift (6). Then, the error in continuous and quantized phase-shifts is defined as $\epsilon_{nl} = \theta^*_{nl} - \hat{\theta}^*_{nl}$. Here, ϵ_{nl} converges to a uniform distribution in the regime of large quantization levels: $\epsilon_{nl} \sim \mathcal{U}[-\tau, \tau)$, where $\tau = \pi/2^B$ [17]. Thus, the optimal received signal power at D (7) is rewritten with discrete phase-shifts as

$$P^*_r = P\left|\beta_h + \sum_{n\in\mathcal{N}}\sum_{l\in\mathcal{L}} \eta_{nl}\beta_{v_{nl}}\beta_{u_{nl}} \mathrm{e}^{j\epsilon_{nl}}\right|^2 = P\left((\beta_h + \Lambda_R)^2 + \Lambda_I^2\right), \quad (8)$$

where $\Lambda_R = \sum_{n\in\mathcal{N}}\sum_{l\in\mathcal{L}} \eta_{nl}\beta_{v_{nl}}\beta_{u_{nl}}\cos(\epsilon_{nl})$ and $\Lambda_I = \sum_{n\in\mathcal{N}}\sum_{l\in\mathcal{L}} \eta_{nl}\beta_{v_{nl}}\beta_{u_{nl}}\sin(\epsilon_{nl})$.

III. Performance analysis

A. The harvested energy

During the $\alpha\tau_d$ portion of S-to-D transmission, D harvests energy based on the TS protocol. Similarly, during the $(1-\alpha\tau_d)$ portion of S-to-D transmission, D also uses the PS protocol to harvest energy (see Fig. 2). The total HE at D is given as $E_D = \alpha\tau_d\Psi_{EH}(P^*_r) + (1-\alpha)\tau_d\Psi_{EH}(\theta P^*_r)$, where $\Psi_{EH}(\cdot)$ is in (2), and P^*_r is the received power at D (8). The average HE at D is given by

$$\bar{E}_D = \alpha\tau_d\mathbb{E}[\Psi_{EH}(P^*_r)] + (1-\alpha)\tau_d\mathbb{E}[\Psi_{EH}(\theta P^*_r)]. \quad (9)$$

Since the exact closed-form evaluation of (9) is mathematically intractable, we invoke Jensen's inequality to derive a tight upper bound in order to obtain useful insights as

$$\bar{E}_D \le \bar{E}^{ub}_D = \alpha\tau_d\Psi_{EH}(\mathbb{E}[P^*_r]) + (1-\alpha)\tau_d\Psi_{EH}(\theta\mathbb{E}[P^*_r]), \quad (10)$$

where $\mathbb{E}[P^*_r]$ can be derived as

$$\mathbb{E}[P^*_r] = P\left(\mathbb{E}\left[\beta_h^2\right] + 2\mathbb{E}[\beta_h]\,\mathbb{E}[\Lambda_R] + \mathbb{E}\left[\Lambda_R^2\right] + \mathbb{E}\left[\Lambda_I^2\right]\right), \quad (11)$$

where $\mathbb{E}\left[\beta_h^k\right]$ is derived as (see Appendix A)

$$\mathbb{E}\left[\beta_h^k\right] = (\xi_h/m_h)^{k/2}\,\Gamma(m_h + k/2)/\Gamma(m_h) \triangleq \bar{\beta}_h^k, \quad (12)$$

where $\Gamma(s) = \int_0^\infty y^s \mathrm{e}^{-y} dy$ is the Gamma function [18, Eqn. 8.310.1]. Moreover, $\mathbb{E}\left[\Lambda_q^k\right] \triangleq \bar{\Lambda}_q^k$ for $q \in \{R, I\}$ and $k \in \{1, 2\}$ is computed as (see Appendix B)

$$\bar{\Lambda}_R = \sum_{n\in\mathcal{N}}\sum_{l\in\mathcal{L}} \eta_{nl}\vartheta_{nl}(1)\sin(\tau)/\tau, \quad (13a)$$

$$\bar{\Lambda}_R^2 = \sum_{n\in\mathcal{N}}\sum_{l\in\mathcal{L}} \eta_{nl}^2\vartheta_{nl}(2)\left(1/2 + \sin(2\tau)/(4\tau)\right), \quad (13b)$$

$$\bar{\Lambda}_I^2 = \sum_{n\in\mathcal{N}}\sum_{l\in\mathcal{L}} \eta_{nl}^2\vartheta_{nl}(2)\left(1/2 - \sin(2\tau)/(4\tau)\right), \quad (13c)$$

where $\vartheta_{nl}(k)$ is given as

$$\vartheta_{nl}(k) \triangleq \left(\frac{\xi_{u_n}\xi_{v_n}}{m_u m_v}\right)^{k/2} \frac{\Gamma(m_u + k/2)\,\Gamma(m_v + k/2)}{\Gamma(m_u)\,\Gamma(m_v)}. \quad (14)$$

B. Average achievable rate

The optimal SNR at D is derived from (4) by following a similar technique to one we used in (8) as

$$\gamma^* = \hat{\gamma}\left[\beta_h + \sum_{n\in\mathcal{N}}\sum_{l\in\mathcal{L}} \eta_{nl}\beta_{v_{nl}}\beta_{u_{nl}}\mathrm{e}^{j\epsilon_{nl}}\right]^2 = \hat{\gamma}\left((\beta_h + \Lambda_R)^2 + \Lambda_I^2\right), \quad (15)$$

where $\hat{\gamma} = \bar{\gamma}(1-\theta)$, and $\bar{\gamma} = P/\sigma_w$ is the transmit SNR. The average achievable rate is defined as $\mathcal{R} = \Omega\mathbb{E}[\log_2(1+\gamma^*)]$, where the pre-log factor, $\Omega = (1-\alpha)\tau_d/\tau_c$, captures the effective potion of the coherence interval (τ_c) for data transmission. The exact derivation of $\mathcal{R}$ appears mathematically intractable, and thus, we resort to tight upper and lower bounds by invoking Jensen's inequality as $\mathcal{R}_{lb} \le \mathcal{R} \le \mathcal{R}_{ub}$ [19], where $\mathcal{R}_{lb}$ and $\mathcal{R}_{ub}$ are given as

$$\mathcal{R}_{lb} = \Omega\log_2\left(1 + (\mathbb{E}[1/\gamma^*])^{-1}\right) \approx \Omega\log_2\left(1 + (\mathbb{E}[1/\tilde{\gamma}^*])^{-1}\right), \quad (16a)$$

$$\mathcal{R}_{ub} = \Omega\log_2(1 + \mathbb{E}[\gamma^*]) \approx \Omega\log_2(1 + \mathbb{E}[\tilde{\gamma}^*]). \quad (16b)$$

The expectation term in (16b) is derived as

$$\mathbb{E}[\bar{\gamma}^*] = \hat{\gamma}\left(\mathbb{E}\left[\beta_h^2\right] + 2\mathbb{E}[\beta_h]\,\mathbb{E}[\Lambda_R] + \mathbb{E}\left[\Lambda_R^2\right] + \mathbb{E}\left[\Lambda_I^2\right]\right), \quad (17)$$

where $\mathbb{E}\left[\beta_h^k\right]$ and $\mathbb{E}\left[\Lambda_q^k\right]$ for $q \in \{R, I\}$ and $k \in \{1, 2\}$ are computed in (12) and (13), respectively. Next, the expectation term in (16a) is written as $\mathbb{E}[1/\gamma^*] = 1/\mathbb{E}[\gamma^*] + \mathbb{V}\mathrm{ar}[\gamma^*]/(\mathbb{E}[\gamma^*])^3$, where $\mathbb{E}[\gamma^*]$ is computed in (17). Furthermore, $\mathbb{V}\mathrm{ar}[\gamma^*]$ is derived as $\mathbb{V}\mathrm{ar}[\gamma^*] = \hat{\gamma}^2\sum_{k\in C^4}\binom{4}{k}\mathbb{E}\left[\beta_h^{(4-k)}\right]\mathbb{E}\left[\Lambda_r^k\right] + 2\hat{\gamma}^2\sum_{k\in C^2}\binom{2}{k}\mathbb{E}\left[\beta_h^{(2-k)}\right]\mathbb{E}\left[\Lambda_r^k\right]\mathbb{E}\left[\Lambda_i^2\right] + \hat{\gamma}^2\mathbb{E}\left[\Lambda_i^4\right] - (\mathbb{E}[\gamma^*])^2$, where $\mathbb{E}\left[\Lambda_q^k\right] \triangleq \bar{\Lambda}_q^k$ for $q \in \{R, I\}$ and $k \in \{3, 4\}$ is computed as

$$\bar{\Lambda}_R^3 = \sum_{n\in\mathcal{N}}\sum_{l\in\mathcal{L}} \eta_{nl}^3\vartheta_{nl}(3)\left(\frac{\sin(\tau)}{\tau} - \frac{\sin^3(\tau)}{3\tau}\right), \quad (18a)$$

$$\bar{\Lambda}_R^4 = \sum_{n\in\mathcal{N}}\sum_{l\in\mathcal{L}} \eta_{nl}^4\vartheta_{nl}(4)\left(\frac{3}{8} + \frac{\sin(2\tau)}{4\tau} + \frac{\sin(4\tau)}{32\tau}\right), \quad (18b)$$

$$\bar{\Lambda}_I^4 = \sum_{n\in\mathcal{N}}\sum_{l\in\mathcal{L}} \eta_{nl}^4\vartheta_{nl}(4)\left(\frac{3}{8} - \frac{\sin(2\tau)}{4\tau} + \frac{\sin(4\tau)}{32\tau}\right). \quad (18c)$$

By substituting (12), (13), (17), and (18) into (16a) and (16b), tight achievable rate upper/lower can be obtained.

C. Energy-rate trade-off for PS protocol

By referring to Fig. 2, we observe that data transfer and energy harvesting occur in the same time-slot for the PS protocol. By first solving for θ in (10) with $\alpha = 0$, and then substituting θ into (16a) and (16b), the lower and upper bounds for the energy-rate trade-off for the PS protocol are obtained as in (19) and (20), respectively, where $\Psi'_{EH}(z)$ is defined as

$$\Psi'_{EH}(z) = \omega - 1/\mu\ln(\lambda/(z(1-\varsigma) + \lambda\varsigma) - 1), \quad (21)$$

where $\varsigma = 1/(1 + \mathrm{e}^{\mu\omega})$.

D. Energy-rate trade-off for TS protocol

In the TS protocol, the transfer of power and information occurs in two orthogonal time-slots. The energy-rate trade-off upper/lower bounds for the TS protocol are derived by first solving for α in (10) with $\theta = 0$, and then substituting α into (16a) and (16b). Then, the lower and upper bounds for the energy-rate trade-off for the TS protocol are derived as shown in (22) and (23), respectively.

$$\mathcal{R}_{lb,PS} \approx \frac{\tau_d}{\tau_c}\log_2\left(1+\frac{\bar{\gamma}\left(1-\Psi'_{EH}\left(\bar{E}^{ub}_{D,PS}/\tau_d\right)/\mathbb{E}[P_r^*]\right)\left(\bar{\beta}_h^2+2\bar{\beta}_h\bar{\Lambda}_R+\bar{\Lambda}_R^2+\bar{\Lambda}_I^2\right)^3}{\sum_{n\in C^4}\binom{4}{n}\bar{\beta}_h^{(4-n)}\bar{\Lambda}_R^n+2\sum_{n\in C^2}\binom{2}{n}\bar{\beta}_h^{(2-n)}\bar{\Lambda}_R^n\bar{\Lambda}_I^2+\bar{\Lambda}_I^4}\right) \tag{19}$$

$$\mathcal{R}_{ub,PS} \approx \tau_d/\tau_c\log_2\left(1+\bar{\gamma}\left(1-\Psi'_{EH}\left(\bar{E}^{ub}_{D,PS}/\tau_d\right)/\mathbb{E}[P_r^*]\right)\left(\bar{\beta}_h^2+2\bar{\beta}_h\bar{\Lambda}_R+\bar{\Lambda}_R^2+\bar{\Lambda}_I^2\right)\right) \tag{20}$$

$$\mathcal{R}_{lb,TS} \approx \frac{\left(1-\bar{E}^{ub}_{D,TS}\Psi^{-1}_{EH}\left(\mathbb{E}[P_r^*]\right)/\tau_d\right)\tau_d}{\tau_c}\log_2\left(1+\frac{\bar{\gamma}\left(1-\bar{E}^{ub}_{D,PS}\Psi^{-1}_{EH}\left(\mathbb{E}[P_r^*]\right)/\tau_d\right)\left(\bar{\beta}_h^2+2\bar{\beta}_h\bar{\Lambda}_R+\bar{\Lambda}_R^2+\bar{\Lambda}_I^2\right)^3}{\sum_{n\in C^4}\binom{4}{n}\bar{\beta}_h^{(4-n)}\bar{\Lambda}_R^n+2\sum_{n\in C^2}\binom{2}{n}\bar{\beta}_h^{(2-n)}\bar{\Lambda}_R^n\bar{\Lambda}_I^2+\bar{\Lambda}_I^4}\right) \tag{22}$$

$$\mathcal{R}_{ub,TS} \approx \left(1-\bar{E}^{ub}_{D,TS}\Psi^{-1}_{EH}\left(\mathbb{E}[P_r^*]\right)/\tau_d\right)\tau_d/\tau_c\log_2\left(1+\bar{\gamma}\left(\bar{\beta}_h^2+2\bar{\beta}_h\bar{\Lambda}_R+\bar{\Lambda}_R^2+\bar{\Lambda}_I^2\right)\right) \tag{23}$$

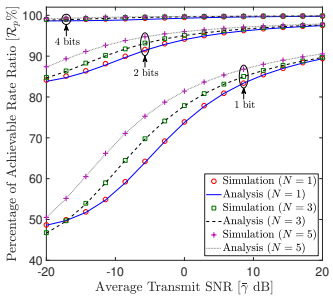

Fig. 3. The effect of discrete phase-shift on the achievable rate for $\alpha = 0.5$, $\theta = 0.5$, and $L = 32$.

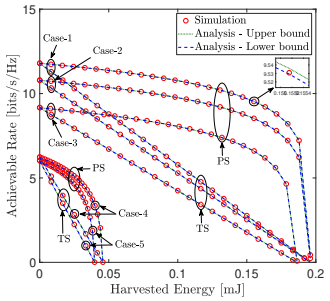

Fig. 4. A comparison of the energy-rate trade-off with different N and L for $B=4$ bits. The combinations of N and L for Case 1 to Case 5 are set to $\{N=3, L=64\}$, $\{N=5, L=32\}$, $\{N=3, L=32\}$, $\{N=3, L=16\}$, and $\{N=1, L=32\}$.

IV. Numerical Results

In simulation, we model the large-scale fading as $\zeta_{ij} = (d_0/d_{ij})^{\nu}\times 10^{\varphi_{ij}/10}$, where $i\in\{S,n\}$ and $j\in\{n,D\}$. The distance between nodes i and j is denoted by d_{ij}, $d_0=1$ m represents a reference distance, $\nu=2.8$ denotes the path-loss exponent, and log-normal shadow fading is captured by $10^{\varphi_{ij}/10}$ with $\varphi_{ij}\sim(0,8)$ [20]. The AWGN variance σ_w^2 is modeled as $\sigma_w^2 = 10\log[10]N_0B_wN_f$ dB, where $N_0=-174$ dBm/Hz, $B_w=20$ MHz is the transmission bandwidth, and $N_f=7$ dB is the noise figure. In the simulation set-up, S and D are placed at fixed locations and separated by 120 m, while the IRSs are uniformly distributed over 100×200 m^2 range. Moreover, $\eta_{nl}=0.9$ for $n\in\mathcal{N}$, $l\in\mathcal{L}$, and $m_h=m_u=m_v=3$.

In Fig. 3, the effects of discrete phase-shifts and the number of quantization bits (B) are investigated by plotting the percentage rate ratio ($\mathcal{R}_p$) as a function of the average transmit SNR ($\bar{\gamma}$) for different number of IRSs defined by $N=\{1,3,5\}$. We define the percentage rate ration as follows: $\mathcal{R}_p=\mathcal{R}_{ub}/\mathcal{R}^c_{ub}\times100\%$, where $\mathcal{R}_{ub}$ is the upper bound of the achievable rate with discrete phase-shift (16b) and $\mathcal{R}^c_{ub}$ denotes the achievable rate upper bound with continuous phase-shifts. We plot Monte-Carlo simulation curves to validate our analysis. Fig. 3 depicts that the effect of discrete phase-shifts at the IRSs can be minimized by adopting a higher B. For example, more than 99% of the achievable rate can be recovered when $B=4$ compared to the continuous phase-shift adjustments at the IRSs. Moreover, a higher number of IRSs is beneficial for improving $\mathcal{R}_p$. For instance, $N=3$ provides a percentage rate ratio gain of 5.5% compared to $N=1$ case for $B=1$ at a transmit SNR of 0 dB. Fig. 3 also shows that $\mathcal{R}_p$ improves in the high transmit SNR regime.

In Fig. 4, the impact of the number of IRSs (N) and number of reflectors (L) on the energy-rate trade-offs of the TS and PS receiver structures is investigated. The trade-off curves for the TS mode are plotted from our analysis in (22) and (23). The trade-off curves for the PS mode are plotted using (19) and (20). Fig. 4 clearly shows that for large combinations of N and L, the energy-rate trade-off can be improved. For example, at a sum rate of 5.0 bits/s/Hz, case-1 and case-2 provide HE gains of 38.0% and 28.4%, respectively, compared the case-3 for the TS mode. Specifically, when the whole time-slot allocated for downlink transmission is used only for data transfer, the achievable rate is maximized as both the TS and PS factors approach zero. Therefore, in this operating point, the HE at D is infinitesimal. As the TS and PS factors approach unity, the HE reaches a maximum, and consequently, the achievable rate vanishes. Thus, Fig. 4 reveals that our analysis is useful in quantifying the fundamental trade-off between the HE and the rate for IRS-assisted SWIPT.

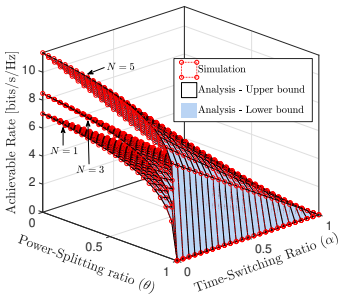

Fig. 5. The achievable rate as a function of the TS and PS ratios for $B=4$ bits, $L=32$, and $\bar{\gamma}=10$ dB.

In Fig. 5 and Fig. 6, the joint effects of the hybrid TS and

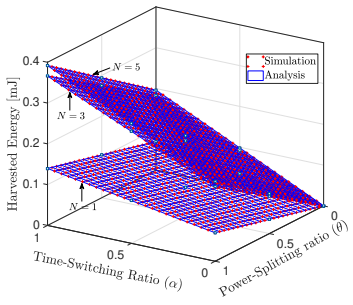

Fig. 6. The total HE as a function of the TS and PS ratios for $B = 4$ bits, $L = 32$, and $\bar{\gamma} = 10$ dB.

PS receiver structure are studied by plotting the achievable rate bounds in (16) and the HE in (10), respectively, as functions of TS (α) and PS (θ) factors. Three sets of rate and HE curves are plotted for $N = \{1, 3, 5\}$. Both Fig. 5 and Fig. 6 reveal that the distributed IRSs deployment outperforms the single IRS set-up in terms of both the achievable rate and the HE. When both α and θ approach unity, the achievable rate becomes infinitesimal (see Fig. 5), whereas the HE becomes maximum (see Fig. 6). Fig. 5 and Fig. 6 are useful in quantifying the performance of distributed IRS-assisted SWIPT with hybrid TS/PS receiver architectures.

V. Conclusion

The feasibility of leveraging distributed IRSs for enhancing the performance gains of SWIPT has been investigated. The optimal received signal/SNR, which is achievable through a distributed IRSs-assisted set-up, has been derived. By adopting a non-linear model and discrete phase-shifts, tight approximations/bounds for the HE, achievable rates, and energy-rate trade-off have been derived in closed-form for Nakagami-m fading. A rigorous set of Monte-Carlo simulations has been presented to validate the accuracy of our theoretical analysis. Our numerical results reveal that a distributed IRSs set-up can be used to improve the performance of SWIPT in the next-generation wireless systems.

Appendix A
The derivation of $\mathbb{E}\left[\beta_h^k\right]$ in (12)

The ith moment of β_h is denoted by $\mathbb{E}\left[\beta_h^i\right]$ and can be computed by using the PDF of β_h as

$$\mathbb{E}\left[\beta_h^k\right] = \int_0^\infty x^k f_h(x)dx = \frac{2m_h^{m_h}}{\Gamma(m_h)\xi_h^{m_h}} \int_0^\infty x^{2m_h+k-1} \mathrm{e}^{-\frac{m_h x^2}{\xi_h}} dx$$
$$\overset{(a)}{=} \xi_h^{k/2} \Gamma\left(m_h + k/2\right) \Big/ \left(\Gamma(m_h) m_h^{k/2}\right), \quad (24)$$

where the step (a) is evaluated by using [18, Eqn. 2.33.10].

Appendix B
The derivation of $\mathbb{E}\left[\Lambda_q^k\right] \triangleq \bar{\Lambda}_q^k$ for $q \in \{R, I\}$

Since $\beta_{u_{nl}}$ and $\beta_{v_{nl}}$ are independent Nakagami-m variables, the $\mathbb{E}[\Lambda_R]$ is derived as

$$\bar{\Lambda}_R = \mathbb{E}\Big[\sum\nolimits_{n\in\mathcal{N}} \sum\nolimits_{l\in\mathcal{L}} \eta_{nl} \beta_{v_{nl}} \beta_{u_{nl}} \cos(\epsilon_{nl})\Big] \quad (25)$$
$$\overset{(b)}{=} \sum\nolimits_{n\in\mathcal{N}} \sum\nolimits_{l\in\mathcal{L}} \eta_{nl} \vartheta_{nl}(1) \sin(\tau)/\tau,$$

where $\vartheta_{nl}(k)$ is defined in (14) and the step (b) is obtained from the fact that ϵ_{nl} is uniformly distributed as $\epsilon_{nl} \sim \mathcal{U}[-\tau, \tau)$. Similarly, we compute $\mathbb{E}[\Lambda_I]$ as

$$\bar{\Lambda}_I = \sum\nolimits_{n\in\mathcal{N}} \sum\nolimits_{l\in\mathcal{L}} \eta_{nl} \mathbb{E}[\beta_{v_{nl}}]\, \mathbb{E}[\beta_{u_{nl}}]\, \mathbb{E}[\sin(\epsilon_{nl})] = 0. \quad (26)$$

Then, $\mathbb{E}\left[\Lambda_R^2\right]$ is derived as

$$\bar{\Lambda}_R^2 = \mathbb{E}\left[\left(\sum\nolimits_{n\in\mathcal{N}} \sum\nolimits_{l\in\mathcal{L}} \eta_{nl} \beta_{v_{nl}} \beta_{u_{nl}} \cos(\epsilon_{nl})\right)^2\right] \quad (27)$$
$$= \sum\nolimits_{n\in\mathcal{N}} \sum\nolimits_{l\in\mathcal{L}} \eta_{nl}^2 \vartheta_{nl}(2) \left(1/2 + \sin(2\tau)/(4\tau)\right).$$

Next, we can evaluate $\mathbb{E}\left[\Lambda_I^2\right]$ by following the similar steps those used in (27) as follows:

$$\bar{\Lambda}_I^2 = \sum\nolimits_{n\in\mathcal{N}} \sum\nolimits_{l\in\mathcal{L}} \eta_{nl}^2 \vartheta_{nl}(2) \left(1/2 - \sin(2\tau)/(4\tau)\right). \quad (28)$$

References

[1] C. Liaskos *et al.*, "A New Wireless Communication Paradigm through Software-Controlled Metasurfaces," *IEEE Commun. Mag.*, vol. 56, no. 9, pp. 162–169, 2018.

[2] M. D. Renzo *et al.*, "Smart Radio Environments Empowered by Reconfigurable AI Meta-Surfaces: An idea whose time has come," *EURASIP J. Wireless Commun. Net.*, May 2019.

[3] D. L. Galappaththige, D. Kudathanthirige, and G. Amarasuriya Aruma Baduge, "Performance Analysis of Distributed Intelligent Reflective Surface Aided Communications," in *IEEE Glob. Commun. Conf. (GLOBECOM)*, May 2020, pp. 1–6, (Accepted).

[4] D. L. Galappaththige, D. Kudathanthirige, and G. Amarasuriya, "Performance Analysis of Distributed Intelligent Reflective Surfaces for Wireless Communications," *arXiv*, 2021.

[5] L. R. Varshney, "Transporting Information and Energy Simultaneously," in *IEEE Int. Symp. Inf. Theory*, 2008, pp. 1612–1616.

[6] R. Zhang and C. K. Ho, "MIMO Broadcasting for Simultaneous Wireless Information and Power Transfer," *IEEE Trans. Wireless Commun.*, vol. 12, no. 5, pp. 1989–2001, 2013.

[7] C. Pan *et al.*, "Intelligent Reflecting Surface Aided MIMO Broadcasting for Simultaneous Wireless Information and Power Transfer," *IEEE J. Sel. Areas Commun.*, vol. 38, no. 8, pp. 1719–1734, 2020.

[8] C. Pan *et al.*, "Reconfigurable Intelligent Surfaces for 6G Systems: Principles, Applications, and Research Directions," *IEEE Commun. Mag.*, vol. 59, no. 6, pp. 14–20, 2021.

[9] Q. Wu, X. Guan, and R. Zhang, "Intelligent Reflecting Surface Aided Wireless Energy and Information Transmission: An Overview," *arXiv*, 2021.

[10] N. Hehao and L. Ni, "Intelligent Reflect Surface Aided Secure Transmission in MIMO Channel with SWIPT," *IEEE Access*, vol. 8, pp. 192 132–192 140, 2020.

[11] Q. Wu and R. Zhang, "Weighted Sum Power Maximization for Intelligent Reflecting Surface Aided SWIPT," *IEEE Wireless Commun. Lett.*, vol. 9, no. 5, pp. 586–590, 2020.

[12] J. Liu *et al.*, "Energy Efficiency in Secure IRS-Aided SWIPT," *IEEE Wireless Commun. Lett.*, vol. 9, no. 11, pp. 1884–1888, 2020.

[13] D. Gunasinghe and G. A. A. Baduge, "Performance Analysis of SWIPT for Intelligent Reflective Surfaces for Wireless Communication," *IEEE Commun. Lett.*, pp. 1–1, 2021.

[14] A. Papoulis and S. U. Pillai, *Probability, Random Variables, and Stochastic Processes*, 4th ed. McGraw Hill, 2002.

[15] E. Boshkovska *et al.*, "Practical Non-linear Energy Harvesting Model and Resource Allocation for SWIPT Systems," *IEEE Commun. Lett.*, vol. 19, no. 12, pp. 2082–2085, Dec 2015.

[16] Q. Wu and R. Zhang, "Intelligent Reflecting Surface Enhanced Wireless Network via Joint Active and Passive Beamforming," *IEEE Trans. Wireless Commun.*, vol. 18, no. 11, pp. 5394–5409, 2019.

[17] S. Haykin and M. Moher, *Communication Systems*, 5th ed. Wiley India Pvt. Limited, 2009.

[18] I. Gradshteyn and I. Ryzhik, *Table of Integrals, Series, and Products*, 7th ed. Academic Press, 2007.

[19] Q. Zhang *et al.*, "Power Scaling of Uplink Massive MIMO Systems with Arbitrary-Rank Channel Means," *IEEE J. Sel. Areas Signal Process.*, vol. 8, no. 5, pp. 966–981, Oct. 2014.

[20] T. L. Marzetta *et al.*, *Fundamentals of Massive MIMO*. Cambridge University Press, Cambridge, UK, 2016.